MDF-Net: Multimodal Dual-Fusion Network for Abnormality Detection using CXR Images and Clinical Data

Chihcheng Hsieh¹, Isabel Blanco Nobre⁴, Sandra Costa Sousa⁴, Chun Ouyang¹, Margot Brereton¹, Jacinto C. Nascimento³, Joaquim Jorge² and Catarina Moreira^{1,2*}

 ¹School of Information Systems, Queensland University of Technology, 2 George St, Brisbane, 4000, QLD, Australia.
 ²INESC-ID / Instituto Superior Técnico, ULisboa, Rua Alves Redol, 9, Lisboa, 1000-029, Portugal.

³Instituto de Sistemas e Robótica, INESC-ID / Instituto Superior Técnico, ULisboa, Rua Alves Redol, 9, Lisboa, 1000-029, Portugal.

⁴Imagiology Department, Grupo Lusíadas, Lisboa, Portugal.

Abstract

This study aims to investigate the effects of including patients' clinical information on the performance of deep learning (DL) classifiers for disease location in chest X-ray images. Although current classifiers achieve high performance using chest X-ray images alone, our interviews with radiologists indicate that clinical data is highly informative and essential for interpreting images and making proper diagnoses. In this work, we propose a novel architecture consisting of two fusion methods that enable the model to simultaneously process patients' clinical data (structured data) and chest X-rays (image data). Since these data modalities are in different dimensional spaces, we propose a spatial arrangement strategy, termed spatialization, to facilitate the multimodal

learning process in a Mask R-CNN model. We performed an extensive experimental evaluation comprising three datasets with different modalities: MIMIC CXR (chest X-ray images), MIMIC IV-ED (patients' clinical data), and REFLACX (annotations of disease locations in chest X-rays). Results show that incorporating patients' clinical data in a DL model together with the proposed fusion methods improves the performance of disease localization in chest X-rays by 12% in terms of Average Precision compared to a standard Mask R-CNN using only chest X-rays. Further ablation studies also emphasize the importance of multimodal DL architectures and the incorporation of patients' clinical data in disease localisation. The architecture proposed in this work is publicly available to promote the scientific reproducibility of our study (https://github.com/ChihchengHsieh/multimodal-abnormalities-detection).

 ${\bf Keywords:}$ Deep Learning, Multimodal Learning, Fusion Methods, Object localisation, Chest X-rays

According to the Lancet [3], 2019 witnessed a shortage of 6.4 million physicians, 30.6 million nurses, and 2.9 million pharmaceutics personnel across 132 countries worldwide, especially in Low and Medium Income Countries. The situation has worsened after the pandemic since medical staff were disproportionately affected.

Deep Learning (DL) technologies promise to deliver benefits for health systems, professionals, and the public, making existing clinical and administrative processes more effective, efficient, and equitable. These technologies have become highly popular in the medical imaging field, where a plethora of applications have been successfully addressed e.g., breast imaging [4, 5], left ventricular assessment [6, 7], dermoscopy analysis [8, 9] and chest X-Rays [10-13], which have gained further attention due to the recent pandemic. Despite their advantages, these systems have notable shortcomings; they require extensive amounts of labeled data to operate correctly. Explicitly labeling anomalies in large amounts of medical images requires the availability of medical experts, who are scarce and expensive. The process is time-consuming and costly, resulting in bottlenecks in research advancements [14]. Additionally, the complex interconnected architectures make DL predictions opaque and resistant to scrutiny, hindering the adoption of AI systems in public health (known as the "black box" problem [15–20]). A system that could automatically annotate or highlight relevant regions in medical images in a similar way to humans would be extremely useful and could save millions of dollars creating breakthroughs in research in AI adoption in Healthcare [14].

Several works in the literature attempt to automatically learn regions of interest indicating the patient's clinical abnormalities. These works mainly use DL approaches which have been found to be efficient and effective on a variety of computer vision tasks [21–24]. Mask R-CNN [25] is one of the most

a) Overall MDF-Net Architecture

Model Output (Predicted lesions)

Feature Extraction Fusion Bounding Box Prediction The state of the

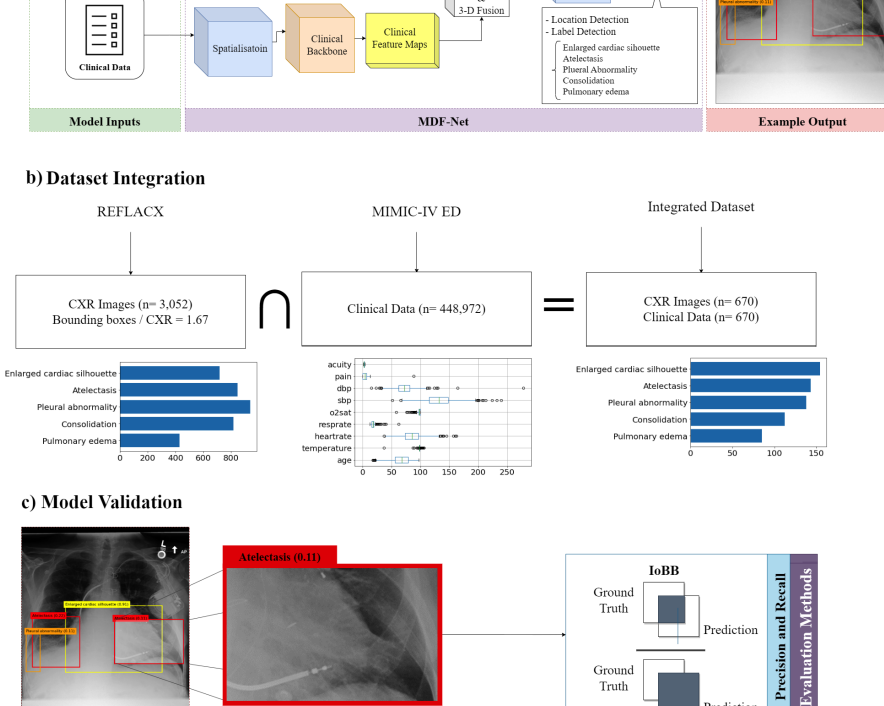


Fig. 1 Panel a) An overview of the proposed MDF-Net architecture. Panel b) Integration of the CXR images from MIMIC-CXR [1] with the clinical data of MIMIC IV [2]. Panel c) IoBB is used to evaluate the model between groundtruths and predictions.

widely used DL architectures to predict regions with abnormalities in images. However, their predictive performance is still low and these architectures do not take into consideration the process of how expert radiologists assess and diagnose these images. The human component is completely disregarded in most DL studies to predict abnormalities in chest X-rays. This is relevant because when radiologists look at an X-ray image they experience it in a multimodal world: they see objects, textures, shapes, etc. It is the combination of these modalities that make humans capable of making mental models that generalize well with less data when compared to DL approaches.

Multimodal DL consists of architectures that can learn, process, and link information from different data modalities (such as text, images, eye-tracking, etc) [26–28]. Deep learning can benefit from multimodal data in terms of generalization and performance compared to the unimodal paradigm [29, 30]. In terms of multimodal DL approaches for chest X-ray images, most works in the literature focus on combining image data with textual reports. The joint representation of these modalities is used to train BERT-like models with several devised domain-specific tasks [31–33]. Another example of multimodal text generation is from Rayner et al. [34] who proposed an architecture consisting of a CNN backbone and two layers of LSTM to construct report texts from given images. The explainability component was incorporated with saliency maps generated by SmoothGrad [35] together with the generated reports.

A recent literature review [36] indicated that clinical data is highly informative and essential for radiologists to interpret and make proper diagnoses. To the best of our knowledge, there are no multimodal DL approaches that combine patients' clinical information with X-ray images to predict the location of abnormalities in chest X-rays. This is relevant, because a clinical feature, such as body temperature, is essential for radiologists to discern whether the patient has a Consolidation or Atelectasis. We argue that incorporating patients' clinical data in a multimodal DL architecture with chest X-ray images will provide better predictions when compared to a DL approach using chest X-rays alone.

In this paper, we propose the Multimodal Dual-Fusion Network (MDF-Net), which is a novel architecture inspired and extended from Mask R-CNN [25]. MDF-Net can fuse chest X-ray images and clinical features simultaneously to detect regions in chest X-rays with abnormalities more accurately. The proposed architecture uses a two-stage detector comprising a Region Proposal Network (RPN) of Mask R-CNN followed by an attention mechanism to extract information only from Regions of Interest (RoIs). Figure 1 presents a general description of the proposed framework. Figure 1 panel a) shows the overall architecture of the proposed model. The prediction process can be divided into 3 phases. The first phase aims to extract the semantics (feature maps) from input data. The two modalities are processed separately. One branch computes a feature map from the input images, and a second branch computes a feature map from clinical data. In the second phase, we conduct a fusion operation to fuse the two feature maps above to obtain a joint representation. Then, the third phase applies the final classifier to predict the bounding boxes of abnormality. In Figure 1 panel b), we integrated the triage data from MIMIC-IV ED with REFLACX in order to get corresponding clinical data for each CXR image. The integrated (multimodal) dataset allows us to perform multimodal learning with the model shown in Figure 1 panel a). In the end, we performed two ablation studies: one that investigated the impact of the different fusion methods in our architecture; and another that investigated the impact of different sets of clinical features for abnormality detection. The

performance of the models was measured using Average Precision (AP) and Intersection Over predicted Bounding Boxes (IoBB) (Figure 1 panel $\bf c$).

The key contributions of this work are as follows:

- 1. We propose a strategy to extract corresponding clinical data for CXR images from the MIMIC [2, 37, 38] dataset. This strategy is then used to construct our own multimodal dataset for the abnormality detection task;
- 2. We propose a multimodal learning architecture and two fusion methods to fuse tabular and image data together;
- 3. We demonstrate the effectiveness and importance of clinical data in abnormality detection through ablation studies.

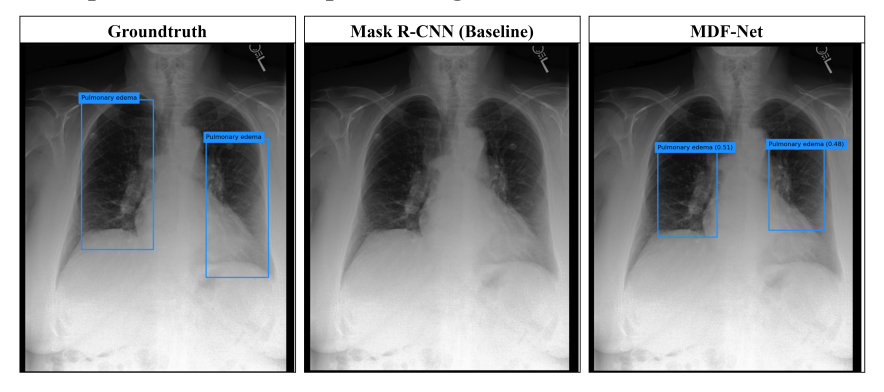
Results

Overall, our experiments show that clinical data plays an important role in abnormality detection. Using clinical data together with chest X-ray images, the proposed MDF-Net architecture achieved a significant improvement when compared to the baseline Mask R-CNN model using X-rays only. Figure 2 panel a) shows an example where the proposed MDF-Net was able to correctly predict a bilateral pulmonary edema while the Mask R-CNN (baseline) did not identify any abnormality. In terms of the number of false negatives/false positives, the proposed MDF-Net with both fusion methods always generated fewer false positives and false negatives for the majority of the chest abnormalities that it was trained on (Figure 2 panel b)). We also performed ablation experiments to evaluate the effectiveness of our fusion methods and the impact of different sets of clinical features. The implementation of this work is open-sourced for further research and reproducibility [39]. However, the dataset is restricted-access and requires users to fulfil PhysioNet's requirements to download and use it.

To evaluate the effectiveness of each fusion method proposed in our MDF-NET, we created two Multimodal Single Fusion Networks (MSF-Net), which only apply 1-D or 3-D fusion to conduct ablation studies. Figure 2 panel c) presents the performance of Mask R-CNN (Baseline), MDF-Net and the two MSF-Nets. Figure 3 panel b) presents the evaluation results across different IoBB thresholds.

We also investigated the impact of different sets of clinical features in the proposed MDF-Net architecture. We first used radiologists' expertise to understand how the different features affect each chest abnormality (Figure 4 panel a)). The radiologists agreed that features such as body temperature are highly relevant for the indication of certain diseases that provoke infections, such as Consolidations or pleural abnormalities. We also investigated if this domain knowledge is present in the dataset by making a correlation analysis between the abnormalities present in each patient and the corresponding clinical data (Figure 4 panel b)). Finally, we applied the proposed MDF-Net and tested it

a) Example of MDF-Net outperforming baseline



b) Confusion Matrix per Abnormailty

Overall			Atelectasis				Consolidation				
	#FP	#FN	#TP		#FP	#FN	#TP		#FP	#FN	#TP
MSF-Net (3D)	167	51	51	MSF-Net (3D)	51	20	15	MSF-Net (3D)	8	9	1
MSF-Net (1D)	103	59	43	MSF-Net (1D)	39	19	16	MSF-Net (1D)	12	7	3
MDF-Net	148	51	51	MDF-Net	36	19	16	MDF-Net	8	9	1
Mask R-CNN (Baseline)	231	53	49	Mask R-CNN (Baseline)	52	21	14	Mask R-CNN (Baseline)	19	9	1
Enlarged cardiac silhouette				Pleural abnormality				Pulmonary edema			
	#FP	#FN	#TP		#FP	#FN	#TP		#FP	#FN	#TP
MSF-Net (3D)	26	1	17	MSF-Net (3D)	31	13	8	MSF-Net (3D)	51	8	10
								A FOR ALL (APA)		1.3	
MSF-Net (1D)	14	3	15	MSF-Net (1D)	15	17	4	MSF-Net (1D)	23	13	3
MSF-Net (ID) MDF-Net	41	0	15 18	MSF-Net (1D) MDF-Net	18	17	5	MDF-Net (ID)	45	7	11

c) Results

Disease	Mask R-CNN (Baseline)		MSF-Net (3D)		MSF-Net (1D)		MDF-Net	
	AP	AR	AP	AR	AP	AR	AP	AR
Enlarged cardiac silhouette	54.8306	100.0000	69.1240	94.4444	50.5422	83.3333	70.3607	100.0000
Atelectasis	14.5784	40.0000	16.3322	42.8571	17.2963	54.2857	24.4309	48.5714
Pleural abnormality	16.2893	42.8571	13.2027	52.3810	10.0843	23.8095	16.0932	28.5714
Consolidation	3.1212	20.0000	16.9346	40.0000	17.5518	30.0000	14.2857	30.0000
Pulmonary edema	9.2211	66.6667	22.2601	72.2222	15.4344	55.5556	33.2543	66.6667
Overall	19.6081	53.9048	27.5707	60.3810	22.1818	49.3968	31.6850	54.7619

Fig. 2 Panel a) The groundtruth and predictions from Mask R-CNN (Baseline) and MDF-Net. In this figure, MDF-Net picked up both pulmonary edema, which our radiologists mentioned the clinical can be helpful on identifying it. Panel b) Confusion matrix per abnormality (Note: The number of true negative cases is infinite in the object detection task). Panel c) Evaluation results (Score threshold = 0.05, IoBB threshold = 0.5).

on different sets of clinical features to investigate their impact in the learning model (Figure 4 panel c)).

Discussion

From the results shown in the previous section, the following findings can be drawn:

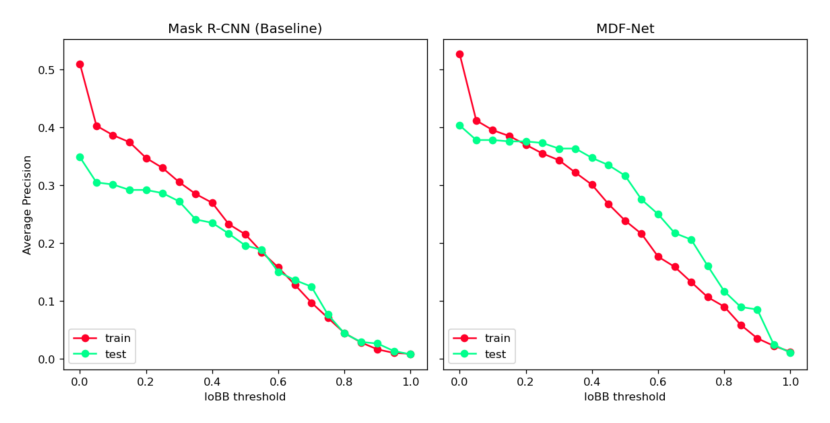
- 1. MDF-Net outperforms the Mask R-CNN (Baseline) on overall AP and AR. MDF-Net has better AP on 4 out of 5 lesions and only has a small difference (-0.17%AP) from the baseline model in detecting *Pleural Abnormality*. In terms of overall performance, MDF-Net yields an improvement of +12% AP and +0.85% AR.
- 2. Figure 3 panel a) shows the model performance on the training set (red) and test set (green). Although both models reached similar performance on the training set, MDF-Net generalised better to the test set compared to Mask R-CNN (Baseline).
- 3. In Figure 3 panel b), MDF-Net (blue) and the other two MSF-Nets outperform Mask R-CNN (purple) on almost all IoBB thresholds. While the Mask R-CNN (Baseline) suffers at a higher IoBB threshold standard, MDF-Net still maintains a reasonable performance, which indicates that MDF-Net can better locate lesions regardless of the IoBB threshold.

From the three findings above, we can experimentally prove that clinical data is of crucial importance and, thus, move away from the idea that using images alone can indicate reliable medical diagnosis.

Ablation Study for fusion methods. The Average Precision (AP) and Average Recall (AR) of each model are shown in Figure 2 panel c). In the previous subsection, we demonstrated the effectiveness of MDF-Net, and in this section, we use MSF-Net (1D) and MST-Net (3D) to conduct an ablation study. This experiment allowed us to test the effectiveness of each fusion method. The results are as follows:

- 1. Figure 2 panel c) shows MSF-Net (3D) has a larger improvement in performance (+7.96%AP, +6.47%AR) than MSF-Net (1D), which indicates the 3-D fusion is more effective than 1-D fusion. Compared to Mask R-CNN (Baseline), MSF-Net (3D) has better performance on 4 out of 5 lesions, which is the same as MDF-Net. And, We also noticed this model has the highest AR compared to all other models.
- 2. The MSF-Net (1D) has a slight improvement on AP by +2.58% but loss -4.508% on AR, as shown in Figure 2 panel c). In MSF-Net (1D), the clinical data are only used to be concatenated with flattened RoIs, which means the clinical data are not involved in deciding where the Regions of Interest are (RPN output). In other words, if we split Mask-RCNN into two stages, the first stage determines the regions of interest (RoIs); and the second stage identifies the lesions inside those RoIs. In 1-D fusion, the clinical data is only perceived by the second stage, so the clinical data is not used for identifying

a) Model Generalisation Analysis



b) Average Precision Analysis for Different IoBB Thresholds

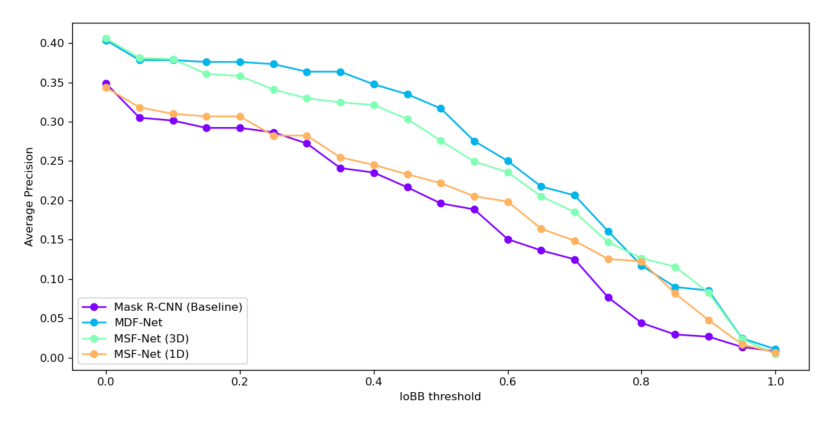


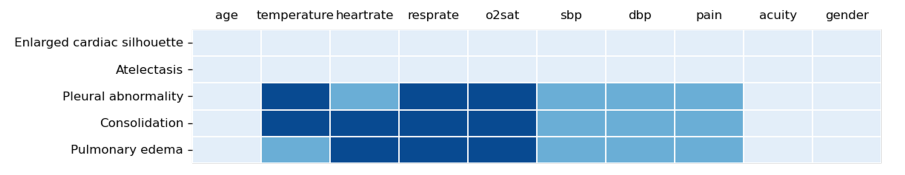
Fig. 3 Panel a) Model generalisation analysis. From this graph, we show that clinical data and MDF-Net improve the generalization ability on the test set. Panel b) Average precision analysis for different IoBB thresholds: This chart shows MDF-Net reached the best performance when using both fusion methods. Only using 1-D or 3-D fusion methods alone can improve the model among all IoBB thresholds.

RoIs. Consequently, this 1-D fusion only helps the final classifier to filter out regions misclassified by RPN; hence, AP increased while AR decreased.

3. When using both 1-D and 3-D fusions together, the 3-D fusion can help RPN to pick up abnormal regions better while 1-D fusion can help the final classifier to determine whether a lesion exists in the given region.

Ablation Study for Clinical features. In order to understand the contribution and significance of clinical features, we also conducted an ablation study by giving a different combination of clinical features to MDF-Net. The performance of different combinations are shown in Figure 4 panel c). When comparing the ablation result with the necessity table (Figures 4 panel a) and 4 panel c) and correlation matrix (Figure 4 panel b), we found:

a) Clinical Data Relevance per Chest Abnormality



b) Correlation Analysis between Clinical Data and Chest Abnormalities



c) Ablation Studies using MDF-Net with Different Sets of Clinical Features

Experiments	Metrics	Enl. Card. Silhouette	Atalectasis	Pleural Abnormality	Consol.	Pulm. Edema	Overall
All Feat.	AP	70.36	24.43	16.09	14.29	33.25	31.69
All Feat.	AR	100.00	48.57	28.57	30.00	66.67	54.76
All Feat. \{Gender}	AP	71.31	18.02	40.56	10.23	9.33	29.89
	AR	88.89	54.29	52.38	30.00	44.44	54.00
{Gender}	AP	67.67	13.06	12.13	4.80	4.19	20.37
	AR	94.44	51.43	42.86	20.00	33.33	48.41
(Candan Ana)	AP	58.48	22.68	12.89	9.86	15.86	23.95
{Gender, Age}	AR	83.33	51.43	42.86	40.00	61.11	55.75
{Gender, Temp}	AP	54.06	15.15	28.19	12.47	6.91	23.35
{Gender, 1emp}	AR	94.44	48.57	61.91	40.00	44.44	57.87
{Gender, Temp., Age}	AP	62.46	24.72	12.68	0.44	18.27	23.71
{Gender, Temp., Age}	AR	77.78	48.57	42.86	10.00	72.22	50.29
{Gender, Heartrate}	AP	72.16	11.61	21.91	7.10	20.77	26.71
	AR	94.44	42.86	42.86	20.00	61.11	52.25
{Gender, Heartrate, Age}	AP	73.47	18.79	20.41	4.10	15.30	26.41
(Gender, Heartrate, Age)	AR	94.44	48.57	57.14	30.00	72.22	60.48
{Gender, RespRate}	AP	63.97	14.57	22.53	17.49	10.55	25.82
(Gender, Respirate)	AR	88.89	31.43	47.62	40.00	61.11	53.81
{Gender, RespRate, Age}	AP	67.01	18.03	29.25	15.01	10.58	27.98
(Gender, Respirate, Age)	AR	100.00	51.43	57.14	40.00	61.11	61.94

Fig. 4 Panel a) The importance of clinical features for detecting each abnormality as reported by our radiology partners from Lusíadas Knowledge Center. Seven clinical features are highlighted for detecting pleural abnormality, consolidation, and pulmonary edema. Four out of seven highlighted features are considered the most significant. Panel b) Correlation matrix between clinical features and abnormalities. Panel c) Results of several ablation studies with different sets of features. Bold values indicate the best performing model in terms of AP, and the underlined values indicate the best performing model in terms of AR.

• In Figure 4 panel a) radiologists stated that *heartrate* is less important than *temperature* and *resprate* in diagnosing a pleural abnormality. In Figure 4 c), we found

$$AP_{\text{gender,heartrate}} < AP_{\text{gender,resprate}} < AP_{\text{gender, temperature}}$$

which follows the importance shown in the necessity table (Figures 4 panel a)). However, when we introduce the *age* feature, we obtain the following inequalities,

$$AP_{\text{gender,age,temp}} < AP_{\text{gender,age,heartrate}} < AP_{\text{gender,age,resprate}}$$

which indicates that *temperature* and *resprate* did not bring more improvement to the model compared to heartrate when age is also used.

- In terms of diagnosing pulmonary edema, radiologists consider temperature less important than heartrate and resprate. The same pattern as diagnosing pleural abnormality is shown. Heartrate and resprate have higher AP than temperature when age is not used.
- Considering the effect of the feature age, (gender, heartrate) is the only combination that has a slight performance drop (-0.298% AP) when age is introduced. The age improves the ability to detect Atelectasis but damages the performance of diagnosing Consolidation. In terms of overall performance, age gains improvement in most of the combinations, which is the same pattern shown in Figure 4 panel b) that age has a higher correlation to most of the abnormalities.
- Moreover, in the same correlation matrix, we noticed the correlation between Consolidation and *resprate* is higher than *heartrate* and o2sat, and the ablation results also show *resprate* improves models the most. Lastly, although *resprate* has a high correlation with enlarged cardiac silhouette, the feature *heartrate* seems more important in determining this abnormality.

Conclusion

In this paper, we propose a MDF-Net and two fusion methods for multimodal abnormality detection, which can perceive clinical data and CXR images simultaneously. In MDF-Net, a spatialisation module is introduced to transform 1-D clinical data to 3-D space, which allows us to predict proposals with multimodal data. And, 1-D fusion is also used to provide clinical information to the final classifier in a residual manner. To test the performance of MDF-NET, we also propose a joining strategy to construct a multimodal dataset for MIMIC-IV. The experiments show that MDF-Net consistently and considerably outperforms the Mask R-CNN (Baseline) mode. And, both fusion methods show significant improvements on Average Precision (AP)

while applying them together can achieve the best performance.

In the future, we will explore the following directions:

- (1) In this work, we can only retrieve 670 instances for our multimodal dataset, which is considered small compared to other popular datasets used for X-ray diagnosis. If there are larger-scaled datasets with clinical data available in the future, our work should also be tested on them to have a more objective evaluation.
- 2. (2) Our fusion methods can also be applied to other models, such as YOLO[40], SSD[41] and DETR[42]. We will incorporate other architectures to evaluate the effectiveness of our fusion methods.

Methods

Model Architecture. In this paper, we propose a new architecture, MDF-Net. Figure 5 panel a) shows the architecture of the original Mask R-CNN, which is the baseline model used in this work. The backbone can be any neural network that can extract feature maps from an image. The architecture of MDF-Net is shown in Figure 5 panel b). Considering the size of dataset, a small pretrained backbone model, MobileNetv3 [43], is used in both Mask R-CNN (baseline) and MDF-Net to prevent overfitting. The parameters used in the network can be found in Table 1.

Input Layer. The proposed network receives as input two different modalities: a front (AP or anterior-posterior view) view of CXR images and the respective clinical data. They are defined as:

- a set of CXR images: $X^{\text{CXR}} \in \mathbb{R}^{W \times H \times C}$;
- a set of clinical data (numerical features): $X^{C_{\text{num}}} \in \mathbb{R}^{n_1 \times 1}$;
- a set of clinical data (categorical features): $X^{C_{\text{cat}}} \in \{0,1\}^{n_2 \times 1}$.

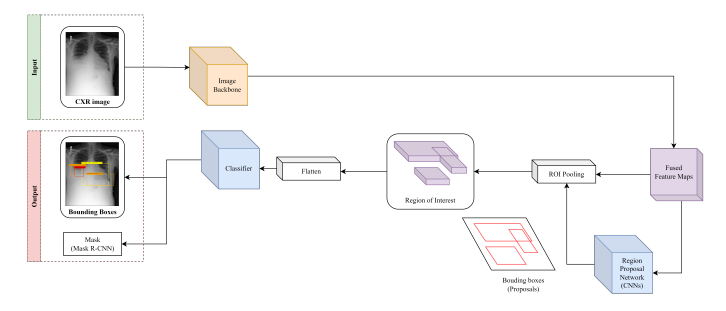
In the proposed architecture, we set the dimensions of our image input space to: W = H = 512, C = 1 (since the CXR image is gray-scale). In terms of the clinical data, our input space corresponds to the number of features: $n_1 = 9$ (continuous variables) and $n_2 = 1$ (categorical variables gender).

Since the input contains modalities with different dimensions, in order to perform fusion, we need to first implement feature engineering in this data to have the same dimensions before attempting any localized object detection learning.

Feature Engineering:
$$\{X^{\mathbf{C}_{\mathbf{num}}}, X^{\mathbf{C}_{\mathbf{cat}}}\} \to \mathcal{C} \in \mathbb{R}^{W' \times H' \times D'}$$
 $X^{\mathbf{CXR}} \to \mathcal{I} \in \mathbb{R}^{W' \times H' \times D'}$

The goal of this step is to transform both the image input data and the clinical data to the same shapes. To achieve this, we do the following:

a) Mask R-CNN (baseline) Architecture



b) MDF-Net Architecture

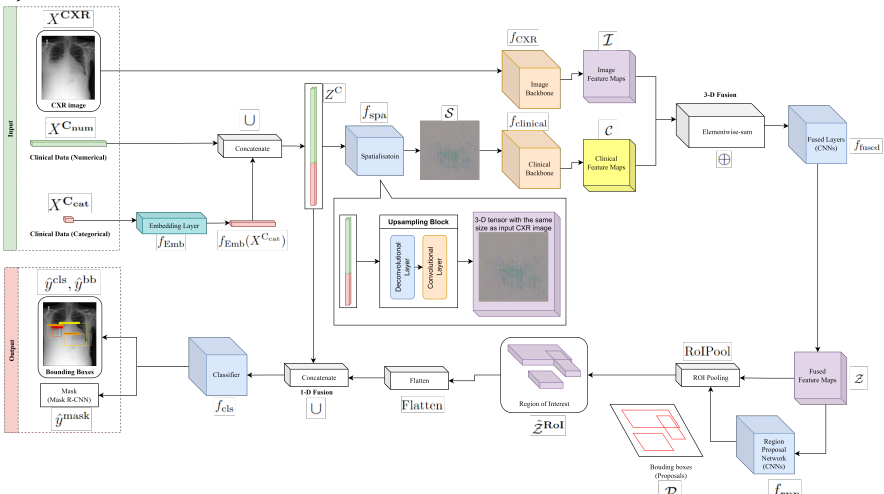


Fig. 5 Panel ${\bf a}$) Mask R-CNN architecture. Panel ${\bf b}$) Our proposed architecture and fusion methods.

1. Image transform: we extracted feature maps from \mathcal{I} using a CNN backbone, f_{CXR} , which in this case corresponds to MobileNetv3 [43]:

$$\mathcal{I} = f_{\text{CXR}}(X^{\text{CXR}}),$$

where the resulting dimensional space is $\mathcal{I} \in \mathbb{R}^{W' \times H' \times D'}$. In our implementation, MobileNetv3 produced the features maps W' = H' = 16, D' = 64. We recognise that MobileNetv3 makes a significant reduction of our feature space, however, when we tried other CNN backbones such as ResNet, we obtained worse results and overfitting. MobileNetv3 provided the best results in our preliminary tests, hence our reason for choosing this backbone.

2. Clinical data encoding: In terms of the feature maps for clinical data, the goal is to concatenate both numerical and categorical feature representations. To do so, we applied an embedding layer to the categorical features, f_{Emb} , so as to obtain a latent vector with the same dimensions of the numerical data. Afterwords, we concatenate the resulting latent vector $f_{\text{Emb}}(X^{C_{cat}})$ with $X^{C_{num}}$ as follows:

$$Z^{\mathcal{C}} = f_{\mathrm{Emb}}(X^{\mathcal{C}_{\mathrm{cat}}}) \cup X^{\mathcal{C}_{\mathrm{num}}}, \text{ where } Z^{\mathcal{C}} \in \mathbb{R}^{n \times 1}, \text{ with } n = n_1 + n_2,$$

where in our implementation n = 64, n1 corresponds to the number of continuous features $(n_1 = 9)$ and n_2 to the number of categorical features after being processed by an embedding layer $(n_2 = 55)$; \cup is the vector concatenation operation. However, the dimensionality \mathcal{C} is different from the generated image feature maps, \mathcal{I} . This required an operation of transforming the dimensions of the clinical data from n times to $W' \times H' \times D'$. To achieve this, we propose a method of spacialisation of the clinical data.

3. **Spatialisation**: We define a spatialisation layer, $f_{\rm spa}$, as a deconvolutional layer [44] followed by a convolution operation. The deconvolution takes as input the $n \times 1$ dimensional clinical data vector and learns an upscaled representation using a sparse encoded convolution kernel [45, 46]. This is given by

$$S = f_{\text{spa}}(Z^C) = f_{L_{\text{spa}}}^e(Z^C), \tag{1}$$

where $f_{L_{\text{spa}}}(Z^C) = f_{\text{conv}}(f_{\text{deconv}}(Z^C))$, and e is the number of spatialised layers (in this work, we set e = 9). After applying spatialisation, the size of S will become $W \times H \times C$, which is the size of input image X^{CXR} .

4. Clinical data transform: The last step for clinical data is to extract the feature maps from spatialised clinical data S. By applying a CNN f_{clinical} , which uses the same architecture as f_{CXR} , we can obtain the clinical feature maps by:

$$C = f_{\text{clinical}}(S).$$

In the end, with the proposed spatialisation operation f_{spa} and the following CNN f_{clinical} , the resulting $\mathcal{C} \in \mathbb{R}^{W' \times H' \times D'}$, which matches the dimensions of \mathcal{I} . From this step, one can proceed to the fusion of both modalities.

Input 3D Fusion: $\{\mathcal{I}, \mathcal{C}\} \to \mathcal{Z} \in \mathbb{R}^{W' \times H' \times D'}$

The final feature map $\mathcal Z$ representing the element wise sum fusion of both modalities is obtained by

$$\mathcal{Z} = f_{\text{fused}}(\mathcal{C} \oplus \mathcal{I}), \ z \in \mathbb{R}^{H' \times W' \times D'},$$
 (2)

where f_{fused} is another CNN module used for obtaining the features maps from the fused modalities, and \oplus corresponds to the element-wise sum operation that

is used for fusion. The final $\mathcal Z$ corresponds to the 3D feature map representation of the combined patient information. Next, we use this data representation as input to a Mask-RCNN architecture to perform abnormality detection.

Region Proposal Network: $\{\mathcal{Z}\} \to \tilde{\mathcal{Z}}^{\mathbf{RoI}} \in \mathbb{R}^{W_r \times H_r}$

To perform localized abnormality detection, we use the Region Proposed Network, f_{rpn} , of Mask-RCNN architecture to generate candidate object bounding boxes also known as proposals \mathcal{P} given by

$$\mathcal{P} = f_{\text{rpn}}(\mathcal{Z}), \forall p_i \in \mathcal{P} : p_i = (x_i, y_i, w_i, h_i, c_i^{\text{obj}}).$$
(3)

RPN learns the coordinates of the generated bounding boxes (x_i, y_i, w_i, h_i) , and the corresponding confidence score, c_{obj} , of having an abnormality (object) in the localization of the bounding boxes. This confidence score is used to sort the generated proposals by their predictive relevance.

Using the coordinates of the computed bounding boxes, a RoIPool operation is performed to extract the corresponding Regions of Interest (RoIs), $\tilde{\mathcal{Z}}^{\text{RoI}} = \text{RoIPool}(\mathcal{P}, \mathcal{Z})$. The RoIs result in a data structure with dimensions $\tilde{\mathcal{Z}}^{\text{RoI}} \in \mathbb{R}^{W_r \times H_r}$, where W_r and H_r are hyper-parameters. In our experiments, we set W_r and H_r to 7.

Output: $\{Z^C, \tilde{\mathcal{Z}}^{\mathbf{RoI}}\} \to \hat{y}$:

After learning the candidate RoIs, we flatten this data to serve as input to a normal dense neural network, which will perform the final classification. In order to emphasize the role of the clinical data in this classification process, we concatenate the clinical data representation, Z^C , with the flattened candidate RoIs, \tilde{Z}^{RoI} , before classification takes place. The role of the 1-Difusion in the MDF-Net is to provide a residual information to further pass the clinical data to deeper layers in our architecture. The final prediction \hat{y} is then obtained by:

$$\hat{y} = f_{\text{cls}}(\text{Flatten}(\tilde{\mathcal{Z}}^{\text{RoI}}) \cup Z^{\text{C}}),$$
 (4)

where \cup represents the vector concatenation operation, $\tilde{\mathcal{Z}}_{RoI} = RoIPool(\mathcal{P}, \mathcal{Z})$, and \hat{y} contains predicted classes \hat{y}^{cls} , bounding boxes \hat{y}^{bb} , binary masks \hat{y}^{mask} , and f_{cls} is the final classification layer.

Training. In the training phase, five loss terms are considered:

- L_{cls} : Cross-entropy between groundtruth abnormality y^{cls} and predicted abnormalities \hat{y}^{cls} . This loss term requires the model to predict the class of abnormalities correctly in the output layer.
- $L_{\rm bb}$: Bounding box regression loss between ground-truth bounding boxes $y^{\rm bb}$ and predicted bounding boxes $\hat{y}^{\rm cls}$ calculated using smooth-L₁ norm:

$$L_{bb} = \sum_{i=1}^{n} l_i, \text{ where } l_i = \begin{cases} 0.5(\hat{y}_i^{\text{bb}} - y_i^{\text{bb}})^2/\beta & \text{, if } \hat{y}_i^{\text{bb}} - y_i^{\text{bb}} < \beta \\ |\hat{y}_i^{\text{bb}} - y_i^{\text{bb}}| - 0.5 * \beta & \text{, otherwise} \end{cases}, (5)$$

 β is a hyperparameter. In our implementation, $\beta = \frac{1}{9}$. To minimise this loss, the model has to locate abnormalities in the correct areas in the output layer.

- L_{mask} : Binary cross-entropy loss between ground-truth segmentation y^{mask} and predicted masks \hat{y}^{mask} , which requires the model to locate abnormalities at pixel level.
- $L_{\text{obj}_{\text{rpn}}}$: Binary cross-entropy loss between ground-truth objectness y^{obj} and predicted objectness c^{obj} (confidence score), which requires RPN to correctly classify whether the proposals (candidate bounding boxes) contain any abnormality.
- $L_{\mathrm{bb_{rpn}}}$: Proposal regression loss between proposals (candidate bounding boxes) $p:p\in\mathcal{P}$ and ground-truth bounding boxes y^{bb} , which is also calculated using the same smooth-L₁ norm function for L_{bb} . This loss term aims to improve RPN on localising abnormalities.

We used homoscedastic (task) uncertainty [47] to train the proposed model using these five loss terms by dynamically weighting them for better convergence. Let $\mathcal{L} = \{L_{\text{cls}}, L_{\text{bb}}, L_{\text{mask}}, L_{\text{obj}_{\text{rpn}}}, L_{\text{bb}_{\text{rpn}}}\}$, we used SGD (stochastic gradient descent) to optimise the overall loss function

$$\arg\min_{\theta,\alpha_l} \sum_{l \in \mathcal{L}} \frac{1}{2\alpha_l^2} l(\theta) + \log \alpha_l^2,$$

where θ is the wights of MDF-Net, and α_l is a trainable parameters to weight each task / loss.

The validation of this architecture required a multimodal dataset. In this study, we used medical data, more specifically chest X-ray images from MIMIC-CXR [37] and patient's clinical data from MIMIC-IV-ED [38]. However, these datasets are offered separately in the literature, and a thorough data integration had to be conducted before evaluating our architecture.

Multimodal Disease Localisation Dataset. As mentioned previously, no existing dataset has both clinical data and CXR images for us to perform multimodal abnormality detection. Therefore, we propose a strategy to combine MIMIC-IV [2] and REFLACX [48] to create our dataset from scratch that meets the requirement of this work. The Medical Information Mart for Intensive Care (MIMIC) IV dataset is sourced from two in-hospital database systems, a custom hospital wide EHR and an ICU specific clinical information system, in Beth Israel Deaconess Medical Center (BIDMC) between 2011 and 2019. The MIMIC-IV database is grouped into three modules, including core, hosp and icu. In this work, only the patients' data in the core module is used.

As well as the MIMIC-IV dataset, two other MIMIC-IV subsets, MIMIC-IV ED (Emergency Department) [38], and MIMIC-IV CXR (Chest X-ray) [37], are used to create the multimodal dataset. These two datasets can be linked to the MIMIC-IV dataset with $subject_id$ and $stay_id$. The MIMIC-IV ED dataset was extracted from the emergency department at the Beth Israel Deaconess

Medical Center. It contains data for emergency department patients collected while they are in the ED. The triage data of the MIMIC-IV ED dataset is one source providing patients' health condition in this work, such as temperature, $heart\ rate$, resprate, etc. MIMIC-CXR is another subset of MIMIC-IV consisting of 227,835 radiographic studies and 377,110 radiographs from BIDMC EHR between 2011 - 2016. In the original MIMIC-CXR dataset, the CXR images are provided in DICOM format, which allows radiologists to adjust the exposure during reading. However, to train a machine learning model, the JPG file is preferred. The author of MIMIC-IV CXR then presented MIMIC-CXR JPG dataset [1] to facilitate the training process. REFLACX dataset is another subset of MIMIC-IV ED, which provides extra data from different modalities, such as eye tracking data, bounding boxes and time-stamped utterances. The bounding boxes in REFLACX are used as groundtruth in this work.

In total ten clinical features are used in this work. The MIMIC-IV Core patients data includes only two clinical attributes, age and gender. And the other eight clinical features are extracted from the MIMI-IV ED traige data. The explanations for these eight clinical features in the MIMIC-IV documentation are:

- 1. **temperature**: The patient's temperature in degrees Farenheit.
- 2. heartrate: The patient's heart rate in beats per minute.
- 3. **resprate**: The patient's respiratory rate in breaths per minute.
- 4. **o2sat**: The patient's peripheral oxygen saturation as a percentage.
- 5. **sbp**, **dbp**: The patient's systolic and diastolic blood pressure, respectively, measured in millimitres of mercury (mmHg).
- 6. **pain**: The level of pain self-reported by the patient, on a scale of 0-10.
- 7. **acuity**: An order of priority. Level 1 is the highest priority, while level 5 is the lowest priority.

Before explaining the creation process, it is necessary to introduce some important IDs and data tables in the MIMIC-IV dataset. Four important IDs are used in MIMIC-IV to link the information across tables. They are:

- **subject_id** (**patient_id**): ID specifying an individual patient.
- stay_id: ID specifying a single emergency department stay for a patient.
- **study_id**: ID specifying a radiology report written for the given chest x-ray. It is rarely mentioned because we do not use the report as the groundtruth label in this paper.
- dicom_id: ID specifying a chest x-ray image (radiograph).

And the following four tables in MIMIC-IV are used to create our multimodal abnormality detection dataset:

• MIMIC-IV Core patients: Information that is consistent for the lifetime of a patient is stored in this table, including age and gender.

- MIMIC-IV ED triage: This table contains information about the patient when they were first triaged in the emergency department, including temperature, heart rate and more clinical data.
- MIMIC-IV Core edstays: Provides the time the patient entered the emergency department and the time they left the emergency department, which helps us to identify the <code>stay_id</code> for CXR images.
- MIMIC-IV CXR metadata: Contains the information about the CXR image (radiograph), including the time taken, high and width.

Data Availability

The code for this work is available on GitHub at https://github.com/ChihchengHsieh/multimodal-abnormalities-detection.

Acknowledgements

This material is based upon work supported by the UNESCO Chair on AI&XR; and the Portuguese *Fundação para a Ciência e a Tecnologia (FCT)* under grants no. 2022.09212.PTDC (XAVIER) and no. UIDB/50021/2020.

Parameter	Value
#Epochs	100
Optimizer	SGD
Learning rate	1e-3
L2 regularization	0
Batch size	4
Fusion Method 1	Element-wise sum
Image Size	512

Table 1 Hyper-parameters used during the training phase.

References

- [1] Johnson, A. E. W. et al. MIMIC-CXR-JPG: A large publicly available database of labeled chest radiographs. CoRR (2019). https://arxiv.org/abs/1901.07042.
- [2] Johnson, A. et al. Mimic-iv (2021). URL https://physionet.org/content/mimiciv/1.0/.
- [3] Haakenstad, A. et al. Measuring the availability of human resources for health and its relationship to universal health coverage for 204 countries and territories from 1990 to 2019: a systematic analysis for the global burden

- 18 MDF-Net for Abnormality Detection using CXR Images and Clinical Data
 - of disease study 2019 (2022). URL https://doi.org/10.1016/s0140-6736(22) 00532-3.
 - [4] Maicas, G., Bradley, A. P., Nascimento, J. C., Reid, I. & Carneiro, G. Pre and post-hoc diagnosis and interpretation of malignancy from breast DCE-MRI. Medical Image Analysis 58 (2019). https://doi.org/10.1016/j. media.2019.101562.
 - [5] Shen, L. et al. Deep learning to improve breast cancer detection on screening mammography. Scientific Reports 9, 2045–2322 (2019).
 - [6] Liu, X. et al. Deep learning-based automated left ventricular ejection fraction assessment using 2-d echocardiography. Journal of Physiology-Heart and Circulatory Physiology 321, H390-H399 (2020).
 - [7] Medley, D. O., Santiago, C. & Nascimento, J. C. Cycoseg: A cyclic collaborative framework for automated medical image segmentation. IEEE Transactions on Pattern Analysis and Machine Intelligence 44 (11), 8167-8182 (2022). https://doi.org/10.1109/TPAMI.2021.3113077.
 - [8] Pham, T.-C., Luong, C.-M., Hoang, V.-D. & Doucet, A. Ai outperformed every dermatologist in dermoscopic melanoma diagnosis, using an optimized deep-cnn architecture with custom mini-batch logic and loss function. Scientific Reports 11, 17485 (2021).
 - [9] Haenssle, H. et al. Man against machine: diagnostic performance of a deep learning convolutional neural network for dermoscopic melanoma recognition in comparison to 58 dermatologists. Annals of oncology 29, 1836–1842 (2018).
- [10] Irvin, J. et al. Chexpert: A large chest radiograph dataset with uncertainty labels and expert comparison, 590–597 (2019).
- [11] Rajpurkar, P. et al. Chexnet: Radiologist-level pneumonia detection on chest x-rays with deep learning. CoRR abs/1711.05225 (2017). https: //arxiv.org/abs/1711.05225.
- [12] Rajpurkar, P. et al. Deep learning for chest radiograph diagnosis: A retrospective comparison of the chexnext algorithm to practicing radiologists. PLOS Medicine 15 (11), 1–17 (2018). https://doi.org/10.1371/journal. pmed.1002686.
- [13] Yates, E., Yates, L. & Harvey, H. Machine learning "red dot": opensource, cloud, deep convolutional neural networks in chest radiograph binary normality classification. Clinical Radiology 73 (9), 827–831 (2018). https://doi.org/10.1016/j.crad.2018.05.015.

- [14] Rahimi, S., Oktay, O., Alvarez-Valle, J. & Bharadwaj, S. Addressing the exorbitant cost of labeling medical images with active learning (2021).
- [15] Guidotti, R. et al. A survey of methods for explaining black box models. ACM Comput. Surv. 51 (5), 93:1–93:42 (2018).
- [16] Lipton, Z. C. The mythos of model interpretability. ACM Communications **61**, 36–43 (2018) .
- [17] Miller, T. Explanation in artificial intelligence: Insights from the social sciences. *Artificial intelligence* **267**, 1–38 (2019) .
- [18] Moreira, C. et al. Linda-bn: An interpretable probabilistic approach for demystifying black-box predictive models. Decision Support Systems 150, 113561 (2021).
- [19] Sindhgatta, R., Ouyang, C. & Moreira, C. Exploring interpretability for predictive process analytics (2020).
- [20] Chou, Y.-L., Moreira, C., Bruza, P., Ouyang, C. & Jorge, J. Counterfactuals and causability in explainable artificial intelligence: Theory, algorithms, and applications. *Information Fusion* 81, 59–83 (2022).
- [21] Singh, A., Sengupta, S. & Lakshminarayanan, V. Explainable deep learning models in medical image analysis. *Journal of Imaging* **6** (6) (2020) .
- [22] Zhuang, F. et al. A comprehensive survey on transfer learning. CoRR abs/1911.02685 (2019). https://arxiv.org/abs/1911.02685.
- [23] Yuan, Z., Yan, Y., Sonka, M. & Yang, T. Robust deep AUC maximization: A new surrogate loss and empirical studies on medical image classification. *CoRR* **2012.03173** (2020). https://arxiv.org/abs/2012.03173.
- [24] Tang, Y.-X. et al. Automated abnormality classification of chest radiographs using deep convolutional neural networks. npj Digital Medicine 3 (1) (2020). https://doi.org/10.1038/s41746-020-0273-z .
- [25] He, K., Gkioxari, G., Dollár, P. & Girshick, R. B. Mask R-CNN. CoRR 1703.06870 (2017). https://arxiv.org/abs/1703.06870.
- [26] Bayoudh, K., Knani, R., Hamdaoui, F. & Mtibaa, A. A survey on deep multimodal learning for computer vision: advances, trends, applications, and datasets. *The Visual Computer* (2021). https://doi.org/10.1007/ s00371-021-02166-7.
- [27] Lahat, D., Adali, T. & Jutten, C. Multimodal data fusion: An overview of methods, challenges, and prospects. *Proceedings of the IEEE* **103** (9), 1449–1477 (2015).

- MDF-Net for Abnormality Detection using CXR Images and Clinical Data
- [28] Ramachandram, D. & Taylor, G. W. Deep multimodal learning: A survey on recent advances and trends. *IEEE Signal Processing Magazine* **34** (6), 96–108 (2017). https://doi.org/10.1109/MSP.2017.2738401.
- [29] Wang, Y. et al. Deep multimodal fusion by channel exchanging. Advances in Neural Information Processing Systems 33 (2020).
- [30] Badgeley, M. A. et al. Deep learning predicts hip fracture using confounding patient and healthcare variables. NPJ digital medicine $\bf 2$ (1), 1–10 (2019).
- [31] Moon, J. H., Lee, H., Shin, W., Kim, Y.-H. & Choi, E. Multi-modal understanding and generation for medical images and text via vision-language pre-training. *IEEE Journal of Biomedical and Health Informatics* 1–10 (2022) .
- [32] Yan, B. & Pei, M. Clinical-bert: Vision-language pre-training for radiograph diagnosis and reports generation (2022).
- [33] Chen, Z., Li, G. & Wan, X. Align, reason and learn: Enhancing medical vision-and-language pre-training with knowledge, 5152–5161 (2022).
- [34] Oakden-Rayner, L. et al. Producing radiologist-quality reports for interpretable deep learning (2019).
- [35] Smilkov, D., Thorat, N., Kim, B., Viégas, F. B. & Wattenberg, M. Smoothgrad: removing noise by adding noise. CoRR 1706.03825 (2017). https://arxiv.org/abs/1706.03825.
- [36] Castillo, C., Steffens, T., Sim, L. & Caffery, L. The effect of clinical information on radiology reporting: A systematic review. *Journal of Medical Radiation Sciences* 68 (1), 60–74 (2021). https://doi.org/https://doi.org/10.1002/jmrs.424.
- [37] Johnson, A. E. W., Pollard, T., Mark, R., Berkowitz, S. & Horng, S. The mimic-cxr database (2019). URL https://physionet.org/content/mimic-cxr/.
- [38] Johnson, A. et al. Mimic-iv-ed (2021). URL https://physionet.org/content/mimic-iv-ed/1.0/.
- [39] Mdf-net: Multimodal dual fusion net (2022). URL https://anonymous. 4open.science/r/multimodal-abnormalities-detection-D505/README. md.
- [40] Redmon, J., Divvala, S. K., Girshick, R. B. & Farhadi, A. You only look once: Unified, real-time object detection. CoRR 1506.02640 (2015). https://arxiv.org/abs/1506.02640.

- [41] Liu, W. et al. Leibe, B., Matas, J., Sebe, N. & Welling, M. (eds) Ssd: Single shot multibox detector. (eds Leibe, B., Matas, J., Sebe, N. & Welling, M.) Computer Vision – ECCV 2016, 21–37 (Springer International Publishing, Cham, 2016).
- [42] Carion, N. et al. End-to-end object detection with transformers. CoRR 2005.12872 (2020). https://arxiv.org/abs/2005.12872.
- [43] Howard, A. et al. Searching for mobilenetv3. CoRR 1905.02244 (2019). https://arxiv.org/abs/1905.02244.
- [44] Zeiler, M. D., Krishnan, D., Taylor, G. W. & Fergus, R. Deconvolutional networks, 2528–2535 (2010).
- [45] Dumoulin, V. & Visin, F. A guide to convolution arithmetic for deep learning (2016). URL https://arxiv.org/abs/1603.07285.
- [46] Albawi, S., Mohammed, T. A. & Al-Zawi, S. Understanding of a convolutional neural network, 1–6 (2017).
- [47] Kendall, A., Gal, Y. & Cipolla, R. Multi-task learning using uncertainty to weigh losses for scene geometry and semantics. *CoRR* **1705.07115** (2017). https://arxiv.org/abs/1705.07115.
- [48] Bigolin Lanfredi, R. et al. Reflacx, a dataset of reports and eye-tracking data for localization of abnormalities in chest x-rays. Scientific Data 9 (2022).